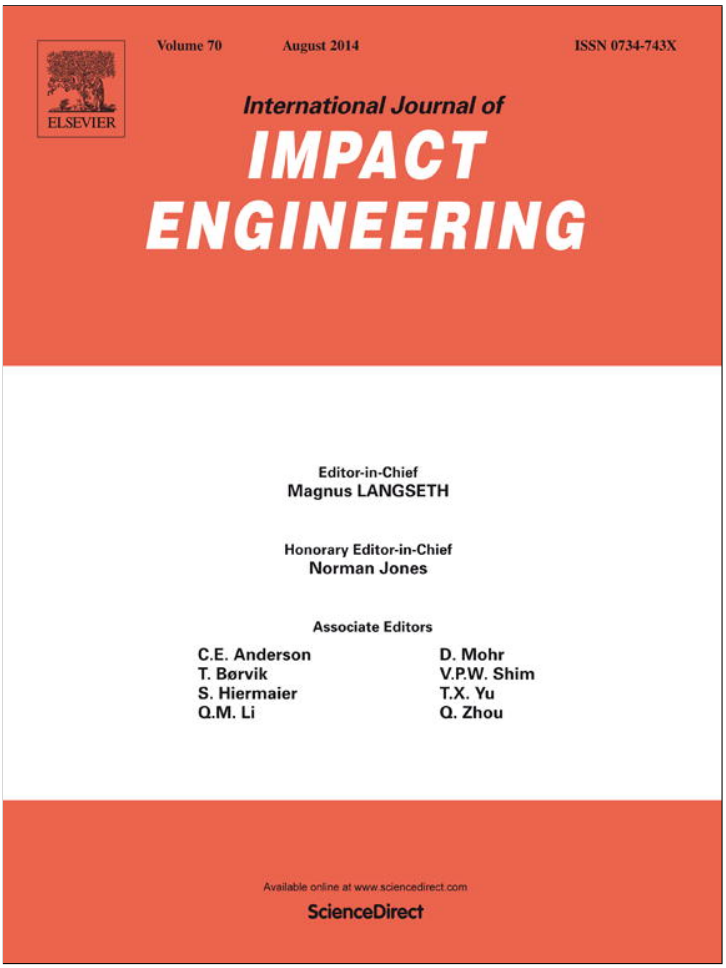

International Journal of Impact Engineering 70 (2014) 50–61

Contents lists available at ScienceDirect

International Journal of Impact Engineering

journal homepage: www.elsevier.com/locate/ijimpeng

Tied interface grid material point method for problems with localized extreme deformation

Y.P. Lian, X. Zhang*, F. Zhang, X.X. Cui

School of Aerospace, Tsinghua University, Beijing 100084, PR China

ARTICLE INFO

Article history:
Received 14 January 2014
Received in revised form
1 March 2014
Accepted 23 March 2014
Available online 3 April 2014

Keywords:
Material point method
Tied interface
Penetration
Contact

ABSTRACT

As a meshless method, the material point method (MPM) is capable of modeling problems with extreme deformation and material fragments. MPM uses a set of Lagrangian particles to discretize a material domain. The interaction between particles is carried out via an Eulerian background grid which is used as a finite element mesh to integrate momentum equations and to calculate spatial derivatives in each time step. Therefore, the accuracy of MPM is mainly dependent on the cell size of the background grid. But, a regular mesh with uniform cells is usually employed as the background grid, which results in poor efficiency for problems with localized extreme deformation. In this article, a tied interface grid material point method is proposed for such problems, in which the background grid with several cell sizes for different sub material domains can be used. The sub grid with refined cell size is used to cover the material domain undergoing extreme deformation, while the sub grid with coarse cell size used to cover the material domain elsewhere. The interaction between refined grid and coarse grid is implemented by a tied interface method. Several numerical examples including stress wave propagation, Taylor bar impact, and penetration problems, are studied to validate the accuracy and efficiency of the proposed method, which shows that the presented method possesses higher efficiency and lower memory requirement than MPM for problems with localized extreme deformation.

1. Introduction

Since the 90s of the last century, meshless/particle methods have attracted more and more attentions due to their capabilities for modeling problems with extreme deformation and material failure, where conventional finite element method (FEM) often encounters mesh distortion and element entanglement. These methods discretize a material domain by particles in the Lagrangian framework, such as the smoothed particle hydrodynamics (SPH) method [1–3], the element free Galerkin (EFG) method [4,5], the reproducing kernel particle method (RKPM) [6,7], material point method (MPM) [8,9], to name just a few. Up to now, these methods and their extensions have been applied successfully to impact/contact/penetration problems [10–14], explosion problems [15–17], crack expansion problems [18–21], fluid solid interaction problems [3,22,23], and so on.

Among the above-mentioned meshless methods, MPM takes advantage of both Lagrangian and Eulerian descriptions, both of which give it the capability of modeling large deformation in a more natural manner. In MPM, a set of Lagrangian particles is used to discretize the material domain; an Eulerian background grid is used as a finite element mesh to integrate the momentum equations and to calculate the spatial derivatives in each time step. At the beginning of each time step, the particles are rigidly attached to the background grid and move with it. Kinematic variables are first mapped from the particles to the grid nodes by nodal shape functions to establish the momentum equations on the background grid. After solving the momentum equations, results are mapped from the grid nodes back to the particles to update their positions and velocities. At the end of each time step, the deformed grid is reset to its initial state for the next time step. Hence, there is no distortion normally associated with FEM, and no material interface tracking difficulties normally associated with Eulerian method. The particles flow through the background grid during the computation process, and their interaction and connection are carried out via the background grid. Furthermore, unlike others meshless methods, the trial functions used in MPM are the same to that of FEM. Therefore, MPM shows some advantages over other meshless methods in efficiency and tension stability [24]. Up to now, significant effort has been devoted to the development of MPM.

* Corresponding author.
E-mail addresses: xzhang@tsinghua.edu.cn, xzhang_thu@163.com (X. Zhang).

http://dx.doi.org/10.1016/j.ijimpeng.2014.03.008
0734-743X/

Several methods [9,25–27] have been proposed to suppress the artificial noise due to the particles moving across the cell boundary, such as the generalized interpolation material point method [9], the convected particle domain interpolation technique [25], the dual domain material point method [26], and so on. Based on the Lagrangian multiplier method, many works have been done to establish the contact/friction/separation algorithm for MPM [14,28,29]. Besides, a series of works have been done to couple MPM with FEM to take fully their advantages by Zhang's group [23,30–32].

Although there is significant effort to extend MPM, few works are devoted to the background grid which is very important due to its significant influence on the efficiency and memory allocated. In any given time step, it is necessary to search the cell in which a particle is located and to calculate the value of grid nodal shape function and its derivative. Generally, a regular grid with uniform cells is adopted as the background grid. The two primary advantages of the regular grid are: (i) the searching is simple with complexity order of $O(N)$, which reduces the computational cost dramatically compared with SPH [24]; and (ii) it could also reduce the computational cost for the shape function and its derivatives calculations. However, there are three obvious disadvantages for the regular grid: (i) it has a limitation to analyze body with arbitrary geometry; (ii) there are many redundant cells which require unnecessary computational cost and memory allocated, because it must be larger than the material domain in space in order to cover the trajectory of all particles; and (iii) it is not optimal for problems with localized extreme deformation or material fragments, where a local refined grid is preferable. To overcome the first disadvantage, Wang et al. [33] proposed an irregular grid scheme with arbitrary quadrilateral cells, where the ray-crossing algorithm is employed to determine the cell in which a particle is located. Wieckowski et al. [34] employed triangular cells in MPM with applications to the silo discharging problem. However, the searching algorithm is till time consuming especially for 3D large scale problems. To overcome the second disadvantage, Ma et al. [24] proposed a dynamic regular grid algorithm, which instantiates only the grid cells containing particles. If all cells connected to a node have not been instantiated, the node will not participate in computation. Therefore, the method could improve the MPM's efficiency and memory requirement. But a regular background grid with uniform cells is still used in Ma's work [24].

To overcome the last disadvantage, a tied interface grid material point method (TIGMPM) is proposed. The background grid is composed of several sub grids with different cell sizes, where the connection and interaction between two adjacent grids are carried out by a tied interface method. In TIGMPM, the background grid covering the material domain undergoing extreme deformation can be refined locally, so the total number of grid cells and particles can be reduced significantly. Furthermore, the moving method of the sub grid with refined cell size is given especially for penetration problems.

The proposed method is first validated by a stress wave propagation problem and a Taylor bar impact problem, and then applied to study the penetration problems. The numerical results are in good agreement with the analytical results and available experimental data, while the efficiency of TIGMPM is much higher than that of MPM for problems with localized extreme deformation.

The remaining part of this article is organized as follows. A brief review of MPM is introduced in Section 2. The tied interface grid MPM is proposed in Section 3, and its numerical implementation is presented in Section 4. The numerical examples are given in Section 5, and the conclusions are summarized in Section 6.

2. Brief review of material point method

As depicted in Fig. 1, the material domain is discretized by a number of particles, which carry all state variables. Because the mass is lumped at each particle, the density can be approximated by

$$\rho(\boldsymbol{x}) = \sum_{p=1}^{n_p} m_p \delta(\boldsymbol{x} - \boldsymbol{x}_p) \tag{1}$$

where p refers to a particle quantity, n_p is the total number of particles, m_p is the mass, $\boldsymbol{x}_p$ is coordinate, δ is the Dirac delta function. The momentum conservation for material domain Ω is

$$\sigma_{ji,j} + \rho b_i = \rho \ddot{u}_i \tag{2}$$

where the subscripts i and j denote the component of the space with Einstein summation convention, the superimposed dot indicates the time derivatives, ρ is the current density, σ_{ij} is the Cauchy stress, b_i is the body force per unit mass, u_i is the displacement. The weak form of Eq. (2) with zero prescribed traction boundary condition is

$$\int_\Omega \rho \ddot{u}_i \delta u_i \mathrm{d}V + \int_\Omega \rho \sigma^s_{ij} \delta u_{i,j} \mathrm{d}V - \int_\Omega \rho b_i \delta u_i \mathrm{d}V = 0 \tag{3}$$

where $\sigma^s_{ij} = \sigma_{ij}/\rho$. Substituting Eq. (1) into Eq. (3) leads to

$$\sum_{p=1}^{n_p} m_p \ddot{u}_{ip} \delta u_{ip} + \sum_{p=1}^{n_p} \frac{m_p}{\rho_p} \sigma_{ijp} \delta u_{ip,j} - \sum_{p=1}^{n_p} m_p b_{ip} \delta u_{ip} = 0 \tag{4}$$

In each time step, particles are rigidly attached to the background grid. The kinematic information can be mapped between particles and grid nodes via the grid nodal shape function. For 3D problems, the 8-point hexahedral cell is usually employed, and therefore the shape function is given as

$$N_{Ip} = \frac{1}{8}(1 + \xi\xi_I)(1 + \eta\eta_I)(1 + \zeta\zeta_I) \quad I = 1, 2, \cdots, 8 \tag{5}$$

where ($\xi \in [-1, 1]$, $\eta \in [-1, 1]$, $\zeta \in [-1, 1]$) are the natural coordinates of particle p. ξ_I, η_I and ζ_I take on their nodal value of (± 1, ± 1, ± 1). The particle displacement u_{ip} and its derivative $u_{ip,j}$ can be interpolated by the grid nodal displacements as

$$u_{ip} = N_{Ip} u_{iI} \tag{6}$$

$$u_{ip,j} = N_{Ip,j} u_{iI} \tag{7}$$

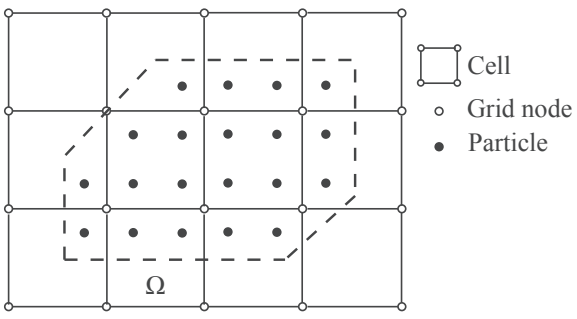

Fig. 1. Sketch of MPM discretization.

where the subscript I refers to a grid node quantity. Substituting Eqs. (6) and (7) into Eq. (4), and invoking the arbitrariness of the nodal virtual displacement δu_{iI} results in

$$\bar{p}_{iI} = f_{iI}^{\text{ext}} + f_{iI}^{\text{int}} \quad I = 1, 2, \cdots, n_g \tag{8}$$

where

$$p_{iI} = m_{Ij}\bar{u}_{ij} \tag{9}$$

is the grid nodal momentum,

$$f_{iI}^{\text{int}} = -\sum_{p=1}^{n_p} N_{Ip,j}\sigma_{ijp}\frac{m_p}{\rho_p} \tag{10}$$

is the grid nodal internal force,

$$f_{iI}^{\text{ext}} = \sum_{p=1}^{n_p} m_p N_{Ip} b_{ip} \tag{11}$$

is the grid nodal external force, and $\sigma_{ijp} = \sigma_{ij}(\boldsymbol{x}_p)$, $b_{ip} = b_i(\boldsymbol{x}_p)$.

If the lumped mass matrix

$$m_I = \sum_{p=1}^{n_p} m_p N_{Ip} \tag{12}$$

is used, Eq. (9) can be rewritten as

$$p_{iI} = m_I \bar{u}_{iI} \tag{13}$$

The leap frog central difference time integration algorithm is used to integrate the momentum equation Eq. (8). In the follows, the superscript k denotes the value of variable at time t^k. Given u_{ip}^k and $\bar{u}_{ip}^{k-1/2}$, we seek for the solution at time t^{k+1}. From Eq. (8), the momentum of grid node can be updated by

$$p_{iI}^{k+1/2} = p_{iI}^{k-1/2} + \left(f_{iI}^{k,\text{ext}} + f_{iI}^{k,\text{int}}\right)\Delta t^k \tag{14}$$

The positions x_{ip}^{k+1} and velocities $v_{ip}^{k+1/2}$ of particle p are updated by

$$x_{ip}^{k+1} = x_{ip}^k + \Delta t^{k+1/2}\sum_{I=1}^{n_g} v_{iI}^{k+1/2} N_{Ip}^k \tag{15}$$

$$v_{ip}^{k+1/2} = v_{ip}^{k-1/2} + \Delta t^k \sum_{I=1}^{n_g} a_{iI}^k N_{Ip}^k \tag{16}$$

where $v_{iI}^{k+1/2} = p_{iI}^{k+1/2}/m_I^k$, and $a_{iI}^k = f_{iI}^k/m_I^k$. After that, all the variables assigned to the grid nodes are reset to zero, which indicates that a new regular background grid is used in the next time step.

In MPM, the particles are taken as quadrature points, and the background grid is embedded in and deform with the material domain only in the current time step. The interaction and connection between particles are carried out via the background grid. The accuracy of the MPM is mainly dependent on the cell size of the background grid, not the particle interval. Therefore, a regular background grid with uniform cells is not optimal for 3D problems involving localized extreme deformation and material failure.

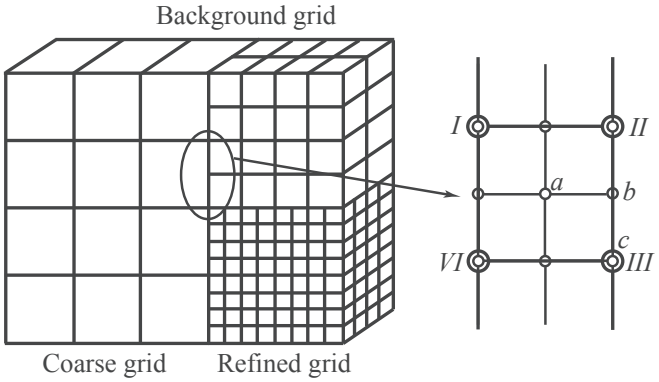

Fig. 2. Tied interface grid.

3. Tied interface grid material point method

In this section, the tied interface grid material point method is proposed. In this method, the background grid is composed of several sub regular grids with different cell sizes. The material domain is discretized by particles with different particle intervals, which is set as half of the cell size of the corresponding sub grid. The refined grid is used to cover the material domain undergoing extreme deformation, while the coarse grid used to cover the material domain elsewhere. The interaction and connection between adjacent grids is implemented by a tied interface method. The particles located in refined grid are referred to as refined particles, while the particles in coarse grid referred to as coarse particles. However, the particles are not fixed to the background grid. In order to track the localized extreme deformation, a method to move the refined grid is proposed. In order to avoid numerical fracture, a particle splitting method is employed to split the coarse particles moving to the refined grid through the tied interface.

3.1. Tied interface method

In each time step, the tied interface is used to link two regular grids with different cell sizes, as shown in Fig. 2. The refined grid nodes located at the interface are referred to as slave nodes, while the coarse grid nodes located at the interface referred to as master nodes. Similarly, the coarse cells located at the interface are referred to as master cells. The cell size ratio between the coarse and refined grids is denoted by R, which is greater than or equal to

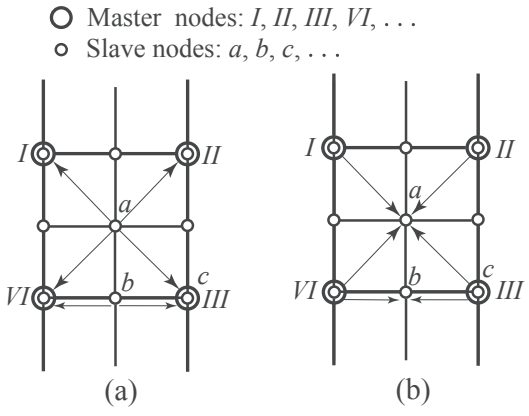

Fig. 3. Tied interface method. (a) map information from slave nodes to master nodes; (b) interpolate information from master nodes to slave nodes.

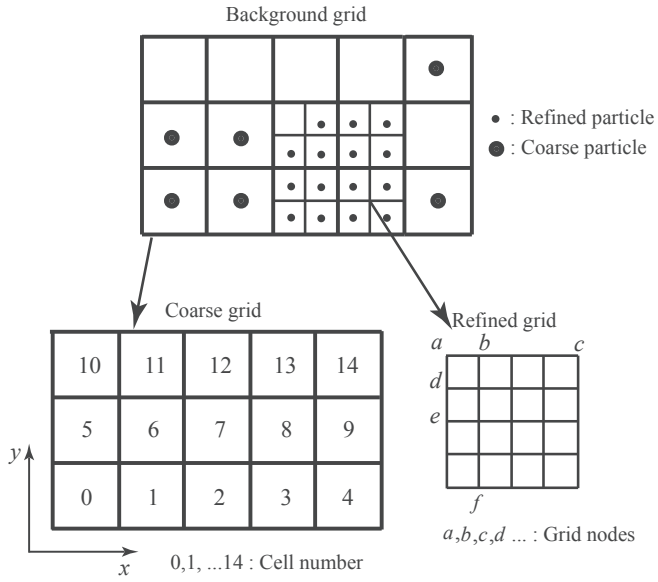

Fig. 4. Tied interface searching: slave nodes and master cells.

1. For example, in Fig. 2, there are three tied interfaces, whose cell size ratio R are 2, 4, and 2, respectively. For the sake of clarity, the tied interface with $R = 2$ is used to illustrate the presented method. Each sub grid has an independent grid nodes set, so there will be grid nodes overlapping at tied interface, such as the node c in the refined grid denoted by small circle and node *III* in the coarse grid denoted by bigger circle, as shown in Fig. 2.

In TIGMPM, the velocity field of the background grid is used to calculate the particle strain rate and to update the particle position, while the acceleration field used to update the particle velocity. Therefore, both velocity and acceleration of slave nodes and master nodes at the interface between two grids must be consistent. In order to connect two grids, the slave nodes are merged to the faces of the master cells by mapping their nodal mass, momentum, and force to the master nodes. After updating the motion of the master

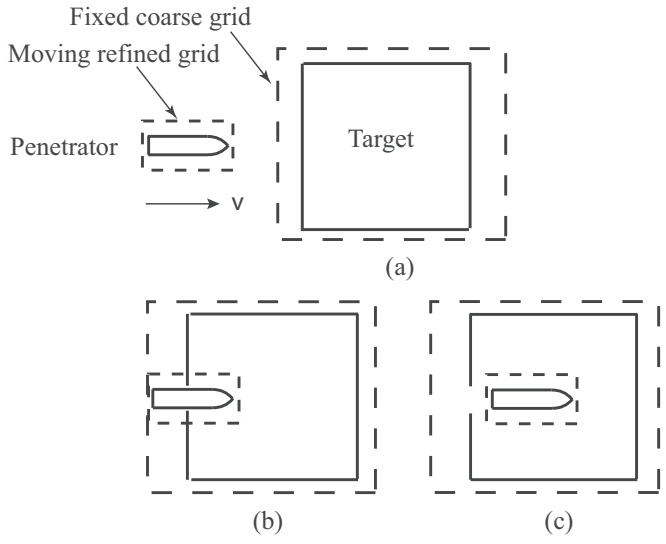

Fig. 5. Sketch of moving refined grid for penetration problems at three different penetration times.

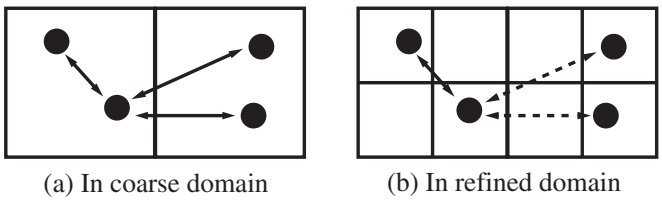

Fig. 6. Numerical fracture.

nodes, the slave nodes move following the master faces, as shown in Fig. 3.

As shown in Fig. 3(a), map the nodal mass and force of the slave nodes onto the master nodes, namely

$$\overline{m}_m^k = m_m^k + \sum_{s=1}^{4} \phi_m(\xi_s, \eta_s) m_s^k \tag{17}$$

$$\overline{\boldsymbol{f}}_m^k = \boldsymbol{f}_m^k + \sum_{s=1}^{4} \phi_m(\xi_s, \eta_s) \boldsymbol{f}_s^k \tag{18}$$

where subscripts m and s refer to a master node quantity and a slave node quantity, respectively. (ξ_s, η_s) is the natural coordinates of the slave node s, and

$$\phi_m(\xi, \eta) = \frac{1}{4}(1 + \xi\xi_m)(1 + \eta\eta_m) \tag{19}$$

is the interpolation function associated with the master node m.

At the beginning of each time step, a new background grid is used, and the grid nodal velocities are obtained by mapping the particles momentum to the grid nodes. Although the velocities of slave nodes and master nodes are consistent at the end of the previous time step, they may not be consistent in the new background grid at the beginning of the current time step. Therefore, it is necessary to remerge the master and slave nodes again by mapping the nodal momentum of slave nodes onto the master nodes by

$$\overline{\boldsymbol{p}}_m^{k-1/2} = \boldsymbol{p}_m^{k-1/2} + \sum_{s=1}^{4} \phi_m(\xi_s, \eta_s) \boldsymbol{p}_s^{k-1/2} \tag{20}$$

Finally, the velocities of the master nodes can be obtained by

$$\boldsymbol{v}_m^{k-1/2} = \frac{\overline{\boldsymbol{p}}_m^{k-1/2}}{\overline{m}_m^{k-1/2}} \tag{21}$$

and the velocities of the slave nodes obtained by

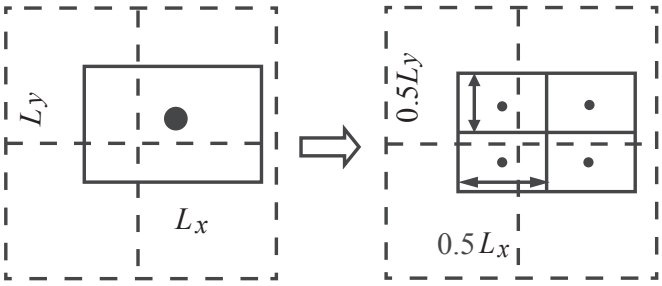

Fig. 7. Particle splitting.

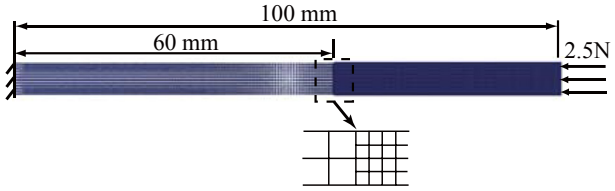

Fig. 8. Discretization model of the rod with $R = 2$.

$$\boldsymbol{v}_s^{k-1/2} = \sum_{m=1}^{4} \phi_m(\xi_s, \eta_s)\boldsymbol{v}_m^{k-1/2} \tag{22}$$

Take the slave node a shown in Fig. 3(b) as an example, $\boldsymbol{v}_m$ is the velocity of the master grid nodes, namely *I*, *II*, *III*, and *VI*. After remerging the master and slave nodes, the velocity fields of both coarse grid and refined grid are consistent at the tied interface, which will be used to calculate the strain rate of particles.

After integrating the momentum equation of the master nodes, the slave nodes move following the master cell surface, namely

$$\boldsymbol{v}_s^{k+1/2} = \boldsymbol{v}_s^{k-1/2} + \boldsymbol{a}_s^k \Delta t^k \tag{23}$$

where the acceleration of the slave node, $\boldsymbol{a}_s^k$, is interpolated from the master grid nodes as

$$\boldsymbol{a}_s^k = \sum_{m=1}^{4} \phi_m(\xi_s, \eta_s)\frac{\bar{\boldsymbol{f}}_m^k}{\bar{m}_m^k} \tag{24}$$

The velocities and accelerations of grid nodes are used to update the positions and velocities of particles, respectively.

3.2. Tied interface searching

In Section 3.1, the slave nodes are tied to the faces of master cells. Tied interface searching method is applied to search the slave nodes and the master cells at the interface between two adjacent grids. A refined grid node will be tied to a master cell only when both the master cell and any cell connected with the refined grid node contain particles at the same time. Therefore, not all the refined grid nodes located at the interface are slave nodes, and not all the coarse cells located at the interface are master cells.

Take a 2D problem shown in Fig. 4 as an example to introduce the searching method in detail. The face nodes of the refined grid, such as *a*, *b*, *c*, *d*, *e*, and *f* are candidates for slave nodes. The coarse cells are numbered from 0 to 14. The refined grid will take the place of coarse cells 2, 3, 7 and 8. The replaced coarse cells are not instantiated and set as virtual cells which won't participate in computation but serve as auxiliary cells to search the coarse cell in which the face nodes is located. Loop over all the face nodes g_s of the refined grid to identify the slave nodes and master cells by the following three steps:

1. Label grid nodes as null nodes if there is no particle located in any cell connected with them. For example, the grid node *a* is a null node. Skip all the null nodes.
2. Search the coarse cell in which the node g_s is located by the following C++ statements

```
NumCellx = int((spanX(2) − spanX(1))/DCell + 0.5)
NumCelly = int((spanY(2) − spanY(1))/DCell + 0.5)
NumCellxy = NumCellx*NumCelly
ix = int((xg − spanX(1))/DCell)
iy = int((yg − spanY(1))/DCell)
iz = int((zg − spanZ(1))/DCell)
InWhichCell = iz*NumCellxy + iy*NumCellx + ix
```

where xg, yg, and zg are the coordinates of node g_s, DCell is the cell size of the coarse grid. spanX, spanY, and spanZ are the minimum and maximum x, y, and z coordinates of the coarse grid. InWhichCell is the index of the cell, which will be termed as iCell hereafter.

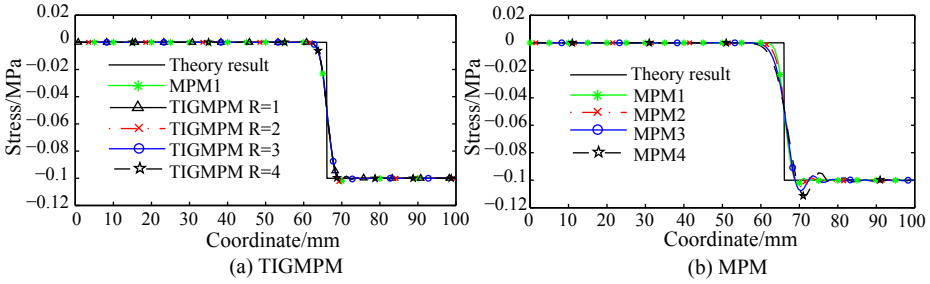

Fig. 9. Elastic stress profiles obtained by TIGMPM and MPM at time $t = 7.6 \times 10^{-3}$ ms.

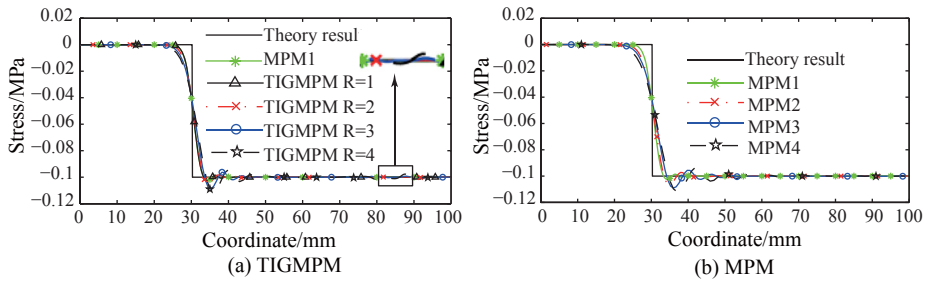

Fig. 10. Elastic stress profiles obtained by TIGMPM and MPM at time $t = 15.6 \times 10^{-3}$ ms.

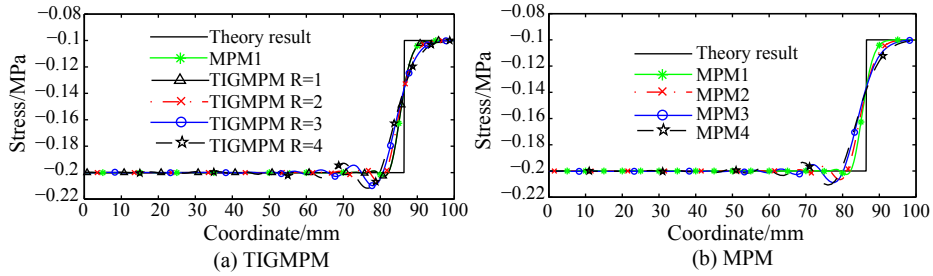

Fig. 11. Elastic stress profiles obtained by TIGMPM and MPM at time $t = 41.6 \times 10^{-3}$ ms.

If the refined grid node g_s is located on a corner of iCell, any cell connected with the corner may be master cell candidates; if the refined grid node g_s is located on a boundary of iCell, any cell connected with the boundary may be master cell candidates. But only the instantiated coarse cells are valid candidates. For the grid node c shown in Fig. 4, iCell is 14, and coarse cells 8, 9, and 13 are connected with the grid node c. However, the coarse cell 8 has been replaced by the refined cells, so the valid candidates are cells 9, 13, and 14. Similarly, cells 1 and 6 are the valid candidates for grid node e, and only cell 6 is the valid candidate for grid node d.

3. Determine the slave nodes and master cells. For master cells, there are particles located in them. The distance between their lower left corner and the node g_s is less than or equal to DCell in x axis direction. Therefore, loop over all valid candidate cells to check if there is any coarse particles located in the cell, and calculate the distance L from the node g_s to the lower left corner of the cell in x axis direction. If there is a coarse particle located in the coarse cell, and L is less than or equal to DCell of the coarse grid, the coarse cell is labeled as a master cell and the node g_s is labeled as a slave node. Once the master cell is found, terminate the loop. For example, the grid nodes c, d, and e are slave nodes, but a, b and f are not. The coarse cells 1, 4, 6, and 14 are master cells. In addition, calculate the natural coordinates of the slave nodes on the surface of the master cell, which will be used in Eqs. (22) and (17).

In 3D problem, the tied interface searching can be conducted in a similar way.

3.3. Moving refined grid

For penetration problems, it is not necessary to use refined grid for the whole material domain which may undergo extreme deformation. As shown in Fig. 5, the size of the penetrator is much smaller than that of the target, and the localized extreme deformation mainly occurs near the contact area between the penetrator and target. Therefore, the refined grid just needs to cover the contact area, and is moved with the penetrator.

In TIGMPM, the refined grid can be moved to track the material domain undergoing localized extreme deformation. During the computation process, the size of the refined grid is fixed. The initial position of the refined grid is set by users. In each time step, the displacement of the refined grid can be determined by $\boldsymbol{L}^k = \boldsymbol{O}_p^k - \boldsymbol{O}_p^{k-1}$, where $\boldsymbol{O}_p^k$ denotes the geometry center of the penetrator at time step k. Considering that the moving distance of the refined grid must be integer times of the cell size of the coarse grid, the actual displacement is $\boldsymbol{M}^k = \text{int}(\boldsymbol{L}^k/\text{DCell})^*\text{DCell}$, and the residual displacement $\boldsymbol{L}^k - \boldsymbol{M}^k$ is accumulated to $\boldsymbol{L}^{k+1}$. Once the refined grid is moved, the background grid cells and nodes should be reset and the tied interface should be researched again.

3.4. Particle splitting method

When coarse particles move to the refined grid, numerical fracture will occur. In TIGMPM, the interaction between particles is carried out via the background grid. If there are empty cells between two particles, there will be no interaction between the two particles, which result in numerical fracture [35], as shown in Fig. 6.

Particle splitting method is proposed to avoid numerical fracture. In the initial discretization, the particle interval is set as half of the cell size of the corresponding grid. Therefore, the particle interval ratio of the coarse particles to the refined particles is also equal to R. When the coarse particles travel into the refined grid, or the refined grid moves into the coarse particles domain, the coarse particle will be split to R^2 and R^3 particles uniformly to avoid numerical fracture for 2D and 3D problems, respectively. The mass, volume, and internal energy of the coarse particle are distributed to the new particles evenly; the stress, strain and other history variables of the new particles are set to those of the coarse particle. Assuming that in the initial configuration each particle represents a cubic, the length of the coarse particle domain in the current configuration can be obtained by its strain as

$$L_i = L_0(1 + \varepsilon_i) \tag{25}$$

where $L_0 = \sqrt[3]{m/\rho}$ is the particle initial length, and ε_i indicates the accumulated strain of the particle in ith direction. In 2D problems, one coarse particle is split to four new refined particles, as shown in Fig. 7.

4. Numerical implementation

A contact/friction/separation algorithm is implemented in TIGMPM to handle the contact event between different bodies. The refined grid is large enough to cover all the contact area, so it is unnecessary to consider the contact conditions at the tied interface. The detail of the contact method is given by Huang et al. [14].

Table 1
The root mean sqaure (RMS) error comparison.

Case	TIGMPM				MPM			
	1	2	3	4	1	2	3	4
Samples Number	400	200	133	100	400	200	133	100
RMS error ($\times 10^{-4}$)	64	68	73	79	64	71	79	87

Table 2
Material constants of Taylor bar.

ρ (g/mm^3)	E (MPa)	ν	A (MPa)	B (MPa)	n	C
8.93×10^{-3}	117×10^3	0.35	157	425	1.0	0.0

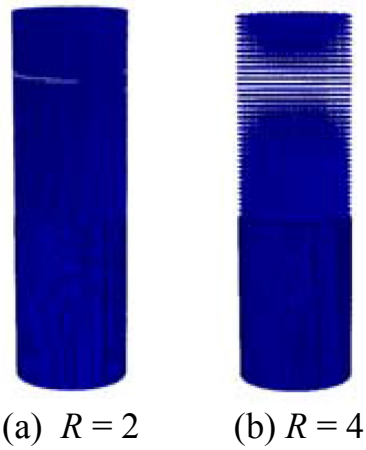

Fig. 12. Discretization models of Taylor bar.

The detailed implementation of TIGMPM is presented here for one time step.

1. Map the mass and momentum of all particles to the background grid. If the particle is located in the refined grid, map its mass and momentum to the refined grid; otherwise map to the coarse grid.
2. Apply boundary conditions on the background grid nodes.
3. Search for the slave nodes and master cells.
4. Map the slave nodal mass and momentum to the master nodes by Eqs. (17) and (20), respectively.
5. Reset the velocities of slave nodes by Eq. (22).
6. Calculate the strain rate and spin tensor of particles, and then update particles stresses.
7. Integrate the momentum equations:
   (a). Calculate the nodal forces of background grid;
   (b). Map nodal force of the slave nodes onto the master grid nodes by Eq. (18);
   (c). Apply boundary conditions on the background grid nodes again;
   (d). Solve the momentum equations on the background grid;
   (e). Reset the acceleration of the slave nodes by Eq. (24) and calculate their velocities by Eq. (23).
8. Update particles positions and velocities by Eqs. (15) and (16), respectively.
9. Move the refined grid by the method presented in Section 3.3, if necessary; redefine the background grid.
10. Split the coarse particles that moved into refined grid by the method presented in Section 3.4.

5. Numerical examples

5.1. Propagation of elastic stress wave

The propagation of elastic stress wave in an elastic rod is studied to validate the accuracy of TIGMPM with different R. The length of the rod is 100 mm and the cross sectional area is 6 mm × 6 mm. The rod is loaded by a force of 2.5 N at the right side and fixed at the other side, as shown in Fig. 8. The density of the rod is set as $\rho = 5$ Kg/m^3, and the elastic parameters are Young's modulus, $E = 100$ GPa, and Poisson ratio, $\nu = 0$. Therefore, the sound speed is $c = \sqrt{E/\rho} = 4472.1$ m/s.

The right part of the rod with length of 40 mm is covered by a refined grid, while the rest part covered by a coarse grid, as shown in Fig. 8. The tied interface position is fixed. Symmetric boundary conditions are applied on the top, bottom, front and back sides of the rod to mimic a 1D problem. Hence, the stress distribution can be obtained analytically from the 1D wave propagation theory. Four cases with $R = 1, 2, 3, 4$ are studied. Fix the cell size of the refined grid as 0.25 mm, while the cell sizes of the coarse grids are 0.25 mm, 0.5 mm, 0.75 mm, and 1 mm in the four cases, respectively. In case with $R = 1$, TIGMPM is equivalent to MPM with cell size 0.25 mm. For comparison, this problem is also solved by MPM with cell sizes 0.25 mm(MPM1), 0.5 mm(MPM2), 0.75(MPM3), and 1 mm(MPM4), respectively.

The stress profiles obtained by TIGMPM and MPM are compared in Figs. 9–11 at three different times for all cases. Fig. 9 shows the stress profiles at time $t = 7.6 \times 10^{-3}$ ms. The wave front travel distance is $l = ct = 33.99$ mm, which is less than the length of the refined grid. The stress wave has not propagated into the coarse grid through the tied interface, so the coarse grid does not influence the result at this time. Therefore, all the results obtained by TIGMPM with different R are the same to those obtained by MPM1, as shown in Fig. 9(a). However, the accuracy of MPM depends on the cell size of the background grid, as shown in Fig. 9(b).

Fig. 10 shows the stress profiles at time $t = 15.6 \times 10^{-3}$ ms. The wave front travel distance is $l = 69.76$ mm, which is longer than the length of the refined grid. At this time, the stress wave has propagated into the coarse grid domain from the refined grid domain. Therefore, the influence of R could be studied. As shown in Fig. 10(a), the stress profiles are different to each other at the wave front with different R. For case with $R = 1$, TIGMPM is equivalent to MPM1. Meanwhile, the oscillation of the stress profile is increased

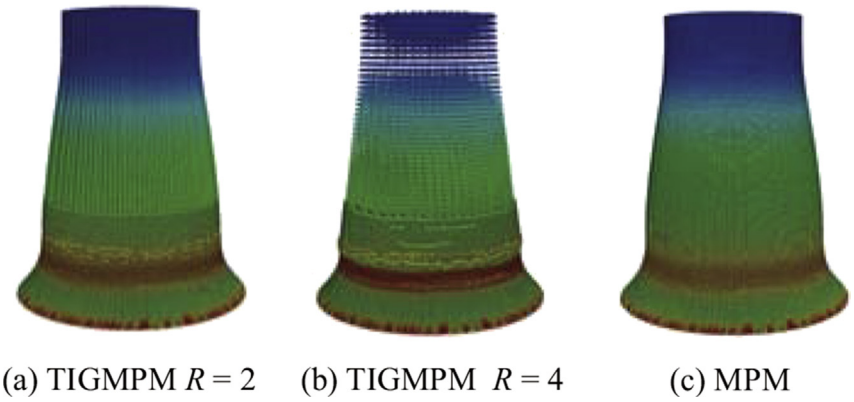

Fig. 13. Final shape of Taylor bar obtained by TIGMPM with different R and MPM with cell size of 0.19 mm.

Table 3
The computational results comparison.

	DCell (mm)/R	L (mm)	D (mm)
Experiment		16.2	13.5
MPM	0.19	16.21	13.28
	0.38	16.29	13.14
	0.76	16.39	12.68
TIGMPM	$R=2$	16.29	13.28
	$R=4$	16.29	13.24

when R increasing, similar to MPM with different cell sizes as shown in Fig. 10(b). Comparing Fig. 10(a) with (b) shows that the accuracy of the TIGMPM is lower than MPM with refined grid but higher than MPM with coarse grid. Furthermore, for case with $R=4$, there is a little oscillation between 80 mm and 90 mm which is far away from the wave front. This is caused by the wave reflection from the tied interface due to the large cell size difference between the refined grid and the coarse grid when the stress wave is propagating from the refined grid to the coarse grid. In addition, Table 1 compares the root mean square (RMS) error for each case, which shows that the result of TIGMPM is better than that of MPM for the cases with same sample points.

Fig. 11 shows the stress profiles at time $t=41.6\times10^{-3}$ ms obtained by TIGMPM and MPM. At this time, the stress wave has reflected from the left side forward to the right side, so the value of the stress wave is doubled due to the fixed boundary conditions. Comparing Fig. 11(a) and (b) shows that the results in the coarse domain obtained by TIGMPM are the same to that by MPM with the same coarse cell sizes. There is no wave reflection from the tied problem interface in case with $R=4$, because the stress wave propagates from the coarse grid into the refined grid.

In summary, before the stress wave reaches to the tied interface, the accuracy of TIGMPM is only dependent on the refined grid cell size. Once the stress wave passes through the tied interface, the accuracy of TIGMPM is between that of MPM with the coarse grid and MPM with the refined grid. In addition, the influence of wave reflection at the tied interface is dependent on the cell size ratio R. When the stress wave travels from the coarse grid into the refined grid, the accuracy of TIGMPM is mainly influenced by the coarse grid cell size.

5.2. Taylor bar impact

The typical Taylor bar test conducted by Johnson et al. [36] is studied, in which a cylinder with an initial velocity of 190 m/s traveled to a rigid wall. The initial length and diameter of the cylinder are $L_0=25.4$ mm and $D_0=7.6$ mm, respectively. Johnson–Cook model is applied for the cylinder with the material constants listed in Table 2 [36].

The discretization model is shown in Fig. 12. The tied interface of the background grid is fixed at 3.8 mm from the bottom of the cylinder. The bottom part of the cylinder is covered by a refined grid, while the top part covered by a coarse grid. Two cases are given. The cell size of the refined grid is 0.19 mm, and R is chosen as 2 and 4 for case I and case II, respectively, as shown in Fig. 12. For comparing, this problem is also simulated by MPM with cell sizes of 0.19 mm (MPM1), 0.38 mm (MPM2), and 0.76 mm (MPM2).

Table 4
The computational cost comparison.

	DCell (mm)/R	End time (ms)	n_p	Total steps	CPU time (s)
MPM	0.19	0.08	1 342 408	3531	9488
	0.38	0.08	169 376	1765	963
	0.76	0.08	21 172	882	27
TIGM	$R=2$	0.08	696 416	3530	5158
	$R=4$	0.08	614 572	3532	3767

Table 5
Material constants of steel.

ρ (g/mm^3)	E (GPa)	ν	A (GPa)	B (GPa)	n	C	c (m/s)	s	γ
7.85×10^{-3}	200	0.3	0.6	0.275	0.36	0	3600	1.9	1.7

The final shapes of the cylinder obtained by TIGMPM and MPM with cell size of 0.19 mm (MPM1) are shown in Fig. 13 in color of equivalent plastic, which shows that Fig. 13(a) is close to Fig. 13(c), but Fig. 13(b) is not very close to Fig. 13(c) due to the big value of $R=4$. Besides, the final bottom diameter D and length L of the deformed cylinder obtained by TIGMPM and MPM are compared with the experimental data in Table 3. The variable D mainly measures the result obtained by the refined grid, while the variable L measures the result obtained by the whole background grid. Therefore, the value of D in case I is very close to MPM1, while the value of L in case I is close to MPM2 due to the influence of the coarse grid. For case II, the value of D is between those obtained by MPM1 and MPM2, while the value of L is very close to that of case I, because the extreme deformation mainly occurs at the bottom of the cylinder.

Furthermore, the CPU time and the total number of particles n_p for all cases are listed in Table 4. The CPU time used by TIGMPM is between that used by MPM with the refined grid and MPM with the coarse grid. Except that, n_p of TIGMPM is smaller than that of MPM with refined grid, so the memory requirement by TIGMPM is smaller than that by MPM.

In summary, the numerical accuracy in the material domain covered by the refined grid can be improved. The results of TIGMPM with $R=2$ are close to MPM1, while the computational cost of TIGMPM is about half of MPM. The results of TIGMPM with $R=4$ are close to TIGMPM with $R=2$, while the CPU time is about 73% of case I. Therefore, the accuracy and efficiency of TIGMPM is dependent on R. But, by comparing the results of case II with MPM2, the computation cost of TIGMPM is expensive with a little accuracy improved, which indicates that TIGMPM is suitable for impact and penetration problems with localized extreme deformation.

5.3. Penetration of steel sphere

A steel sphere penetration problem [14,37] is studied. The sphere impacted to a circular steel plate in its normal direction. The initial velocity of the sphere is 200 m/s. The diameter of the sphere is 10 mm, while the thickness and diameter of the target plate are 1 mm and 178 mm, respectively. Both the sphere and the plate are modeled as an elastic–plastic material, whose deviatoric stress is updated by the Johnson Cook constitutive model, and pressure

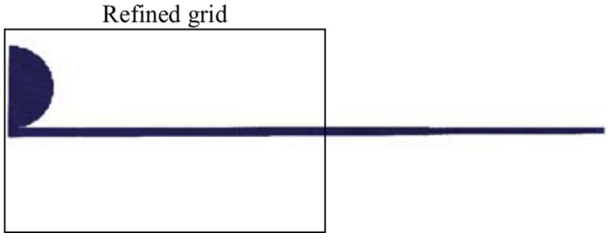

Fig. 14. Discretization model of sphere impacting plate.

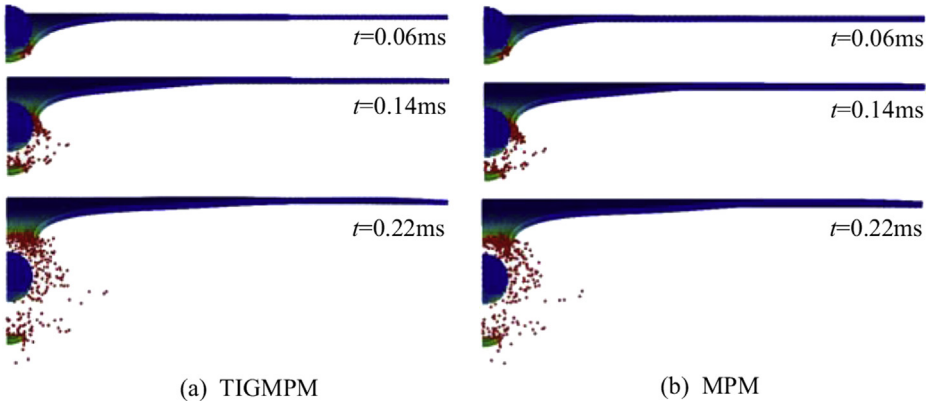

Fig. 15. The configurations at various time step obtained by both TIGMPM and MPM.

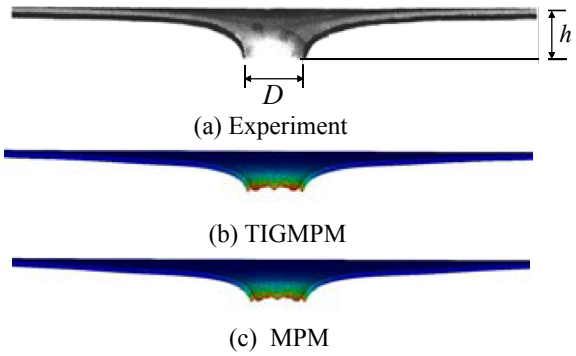

Fig. 16. Final deformed shape of the target plate.

Table 6
The computational results and cost comparison.

	DCell (mm)	h/D	Total particles	Total steps	CPU time (s)
Experiment	–	0.84	–	–	–
MPM	0.5	0.85	404 344	6737	12 314
TIGMPM	0.5/1	0.85	201 074	6737	4875

updated by the Mie–Grüneisen equation of state. The material constants are listed in Table 5 [14]. When the effective plastic strain $\varepsilon_{\text{fail}}$ reaches the strain of 0.5, the deviatoric components of the stress tensor are set to zero to take account of the material failure. The frictional coefficient between the sphere and target is set to zero.

One-fourth of the model is studied due to symmetry. As shown in Fig. 14, the background grid near the sphere is locally refined. The cell sizes of the refined grid and the coarse grid are 1 mm and 2 mm, respectively. The ratio R is 2. For comparing, this problem is also simulated by MPM with the refined cell size of 1 mm.

The configurations in color of equivalent plastic strain at different times obtained by TIGMPM and MPM are compared in Fig. 15, which show that the results agree well with each other. The final configurations of the deformed plate obtained by TIGMPM and MPM are compared with that obtained by the experiment in Fig. 16, where h is the height of the final deformed plate and D is the diameter of penetrated hole. As listed in Table 6, the values of h/D obtained by both methods are the same 0.85, which is close to the experiment value of 0.84. The final shapes of the deformed plate obtained by both TIGMPM and MPM are in good agreement with experiment data, while the CPU time used by TIGMPM is only about 1/3 of that by MPM.

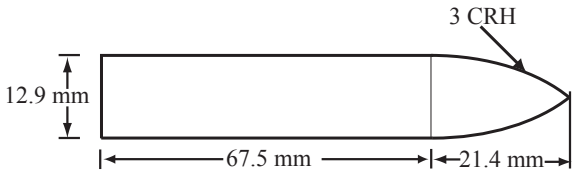

Fig. 17. Schematic of the ogive-nosed projectile.

5.4. Penetration of thick plate

The impact of an ogive-nosed high strength steel projectile against an A6061-T651 thick plate [38] is studied. The projectile has a length of 88.9 mm and a diameter of 12.9 mm with a 3.0 caliber-radius-head, as shown in Fig. 17. The target has a thickness of 26.3 mm and an area of 110×110 mm, and the projectile impacts the target obliquely with an angle of 30°.

In the experiment, the configurations of the projectiles were kept well but with a little permanent deformation after penetration. Hence the projectile is modeled by an elastic–plastic material law with isotropic hardening. The target is modeled by an elastic–plastic material law, whose deviatoric stress is updated by the Johnson Cook constitutive model, and pressure by the Mie–Grüneisen equation of state. The material constants for the projectile and target are listed in Tables 7 and 8 [38,39]. For target, material failure is taken into account by setting the deviatoric components of the stress tensor to zero when the effective plastic strain reaches the strain $\varepsilon_{\text{fail}} = 1.6$. The friction coefficient between projectile and target is set as zero.

Table 7
Material constants of Projectile.

ρ (g/mm^3)	E (GPa)	μ	σ_y (GPa)	E_T (GPa)
0.00785	202	0.3	1.43	14.759

Table 8
Material constants of Target.

ρ (g/m^3)	E (MPa)	μ	A (MPa)	B (MPa)	n	C	m
0.0027	69	0.3	262	52.1	0.41	0	0.859
c_0 (mm/ms)	s	γ_0	T_{melt} (K)	T_{room} (K)			
5350	1.34	2.0	875	293			

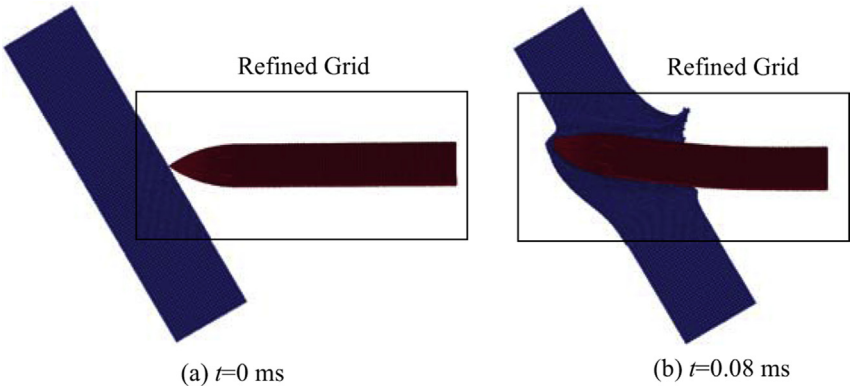

Fig. 18. The positions of refined background grid at different times.

Due to symmetry, one half of the model is studied as shown in Fig. 18(a). The background grid near the projectile is locally refined. The cell sizes of the refined grid and coarse grid are 1 mm and 2 mm, respectively. In this example, the range of the refined grid is set as length of 48 mm in x direction, 24 mm in y direction, and 110 mm in z direction. At the beginning of the simulation, the refined grid is set to cover the whole projectile. Then, it is moved with the geometry center of the projectile throughout the

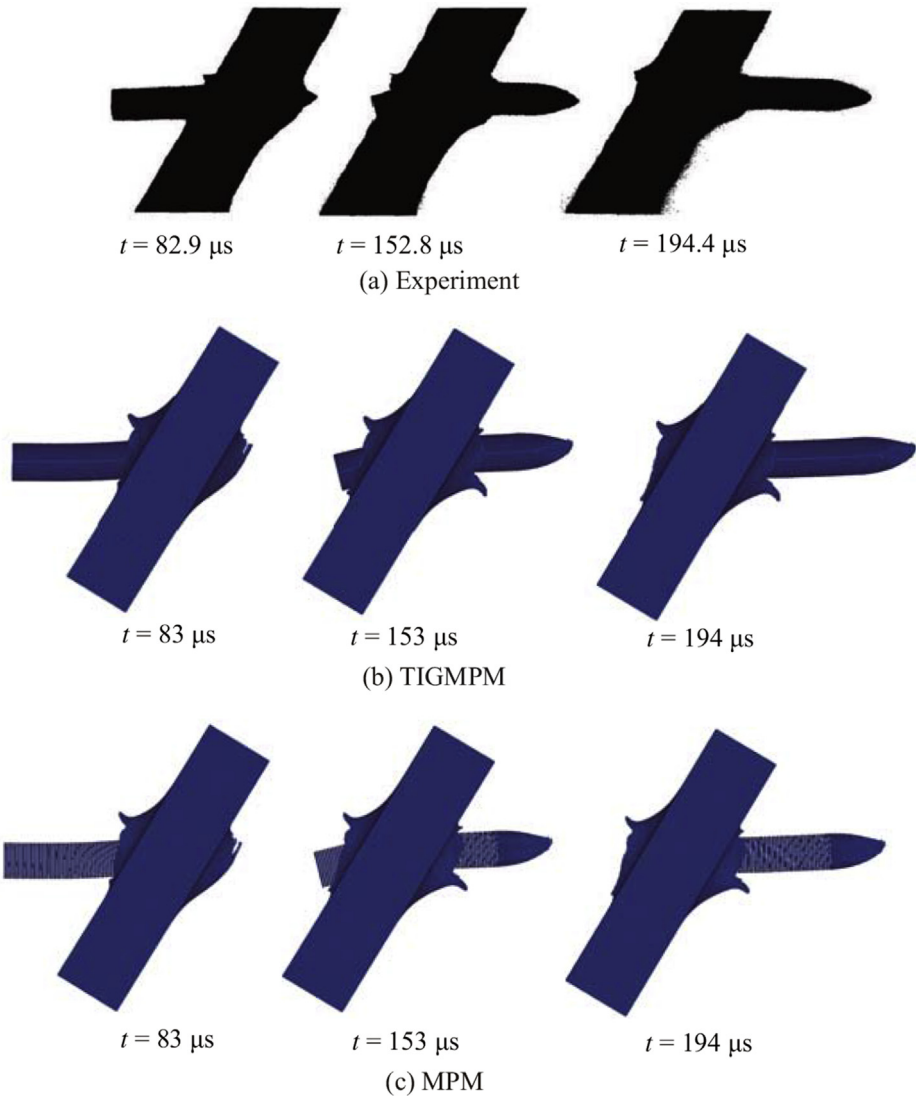

Fig. 19. Projectile-target interactions at three different times with the striking velocity $v_0 = 575$ m/s.

Table 9
The projectile's residual velocities v_r for different striking velocities v_0.

v_0 (m/s)	v_r (m/s)		
	Experiment	TIGMPM	MPM
446	288	299	306
575	455	470	471
730	655	651	652

Table 10
The computation cost comparison.

v_0	End time (ms)	Total steps		CPU time (min)	
		TIGMPM	MPM	TIGMPM	MPM
446	0.4	7652	7679	119	467
575	0.3	5879	5885	95	391
730	0.21	4228	4227	68	258

computational process to track the localized extreme deformation, and therefore more and more particles of the target are split as shown in Fig. 18. Hence the accuracy for the contact between projectile and target is guaranteed by the refined grid and refined particles. For comparison, this problem is also simulated by MPM with the refined cell size of 1 mm.

We focus first on the case with striking velocity, $v_0 = 575$ m/s. The residual velocity of the projectile obtained by TIGMPM and MPM are 470 m/s and 471 m/s, respectively, both of which are in good agreement with the experiment data 455 m/s. Moreover, the projectile–target interactions at three impact times are compared in Fig. 19, where Fig. 19(a) shows the results obtained by experiment, Fig. 19(b) by TIGMPM, and Fig. 19(c) by MPM. The projectile's shapes obtained by TIGMPM and MPM are consistent with the experimental results at the three impact times.

Furthermore, the projectiles with different striking velocities are investigated with the same background grid used above. With different initial velocities, the time needed by projectile to penetrate the plate is different. So, the end time setting for each case is different. The residual velocities of the projectiles obtained by TIGMPM and MPM are listed in Table 9, which shows that the numerical results agree well with the experimental data. The residual velocities obtained by TIGMPM are less than that by MPM due to the tied interface and the coarse grid. However, the difference between two methods is negligible. The efficiency of TIGMPM is much higher than that of MPM as shown in Table 10, while the steps used by both methods are close to each other. The increasing efficiency factor is not a determinate number for different cases due to different parameters such as initial velocity and end time.

6. Conclusion

Different with other meshless methods, material point method (MPM) uses two descriptions to discretize material domain, a set of Lagrangian particles and an Eulerian background grid. The accuracy of MPM mainly depends on the cell size of the background grid, and the computational cost is related to the total number particles and cells used in MPM. MPM usually employs a uniform regular background grid with a uniform particles discretization, which makes it time consuming and memory consuming for problems with localized extreme deformation, where refined grid and refined particles are only needed in the local material domain.

In order to avoid the shortcomings of MPM, a tied interface grid material point method (TIGMPM) is proposed, in which the background grid could be composed of several sub regular grids with different cell sizes. By this method, the background grid and particles covering the material domain undergoing localized extreme deformation are locally refined. The interaction between adjacent sub grids is implemented via a tied interface method. Furthermore, the refined grid could be moved to track the material domain involving extreme deformation. A series of numerical examples are studied, which show that the efficiency of TIGMPM is much higher than that of MPM, and the accuracy is close to that of MPM with refined mesh for whole material domain.

Acknowledgments

This work is supported by the Project funded by China Postdoctoral Science Foundation (2013M530040), National Basic Research Program of China (2010CB832701), and National Natural Science Foundation of China (11390363).

References

[1] Monaghan JJ. An introduction to SPH. Comput Phys Commun 1988;48:89–96.
[2] Liu MB, Liu GR. Smoothed particle hydrodynamics (SPH): an overview and recent developments. Arch Comput Methods Eng 2010;17:25–76.
[3] Rafiee A, Thiagarajan KP. An SPH projection method for simulating fluid-hypoelastic structure interaction. Comput Methods App Mech Eng 2009;198(33–36):2785–95.
[4] Belytschko T, Lu YY, Gu L. Element free Galerkin methods. Int J Numer Methods Eng 1994;37:229–56.
[5] Pan XF, Yuan H. Computational algorithm and application of element-free Galerkin methods for nonlocal damage models. Eng Fract Mech 2010;77:2640–53.
[6] Liu WK, Chen YJ. Wavelet and multiple scale reproducing kernel methods. Int J Numer Methods Fluids 1995;21(10):901–31.
[7] Chen JS, Pan C, Roque CMOL, Wang HP. A Lagrangian reproducing kernel particle method for metal form analysis. Comput Mech 1998;22(3):289–307.
[8] Sulsky D, Chen Z, Schreyer HL. A particle method for history-dependent materials. Comput Methods App Mech Eng 1994;118(1–2):179–96.
[9] Bardenhagen SG, Kober EM. The generalized interpolation material point method. Comput Model Eng Sci 2004;5(6):477–95.
[10] Chen JS, Pan CH, Wu CT. Application of reproducing kernel particle method to large deformation contact analysis of elastomers. Rubber Chem Technol 1998;71(2):191–213.
[11] Rabczuk T, Eibl J. Modeling dynamic failure of concrete with meshfree methods. Int J Impact Eng 2006;32:1878–97.
[12] Vignjevic R, De Vuyst T, Campbell JC. A frictionless contact algorithm for meshless methods. Comput Model Eng Sci 2006;13(1):35–47.
[13] Gan Y, Chen Z, Montgomery-Smith S. Improved material point method for simulating the zona failure response in piezo-assisted intracytoplasmic sperm injection. Comput Model Eng Sci 2011;73(1):45–76.
[14] Huang P, Zhang X, Ma S, Huang X. Contact algorithms for the material point method in impact and penetration simulation. Int J Numer Methods Eng 2011;85(4):498–517.
[15] Liu MB, Liu GR, Zong Z, Lam KY. Computer simulation of high explosive explosion using smoothed particle hydrodynamics methodology. Comput Fluids 2003;32(3):305–22.
[16] Lian YP, Zhang X, Zhou X, Ma S, Zhao YL. Numerical simulation of explosively driven metal by material point method. Int J Impact Eng 2011;38:237–45.
[17] Yang PF, Liu Y, Zhang X, Zhou X, Zhao YL. Simulation of fragmentation with material point method based on Gurson model and random failure. Comput Model Eng Sci 2012;85(3):207–36.
[18] Rabczuk T, Belytschko T. Application of mesh free methods to static fracture of reinforced concrete structures. Int J Fract 2006;137:19–49.
[19] Nairn JA. On the calculation of energy release rates for cracked laminates with residual stresses. Int J Fract 2006;139:267–93.
[20] Tian R, Albert CT, Liu WK. Conforming local meshfree method. Int J Numer Methods Eng 2011;86(3):335–57.
[21] Yang PF, Gan Y, Zhang X, Chen Z, Qi WJ, Liu P. Improved decohesion modeling with the material point method for simulating crack evolution. Int J Fract 2014;186:177–84.
[22] Idelsohn SR, Marti J, Limache A, Onate E. Unified Lagrangian formulation for elastic solids and incompressible fluids: application to fluid-structure interaction problems via the PFEM. Comput Methods App Mech Eng 2008;197(19–20):1762–76.
[23] Lian YP, Zhang X, Liu Y. Coupling of finite element method with material point method by local multi-mesh contact method. Comput Methods App Mech Eng 2011;200:3482–94.
[24] Ma S, Zhang X, Qiu XM. Comparison study of MPM and SPH in modeling hypervelocity impact problems. Int J Impact Eng 2009;36:272–82.
[25] Sadeghirad A, Brannon RM, Burghardt J. A convected particle domain interpolation technique to extend applicability of the material point method for

problems involving massive de-formations. Int J Numer Methods Eng 2011;86:1435–56.
[26] Zhang DZ, Ma X, Giguere PT. Material point method enhanced by modified gradient of shape function. J Comput Phys 2011;230:6379–98.
[27] Mast CM, Mackenzie-Helnwein P, Arduino P, Miller GR, Shin W. Mitigating kinematic locking in the material point method. J Comput Phys 2012;231:5351–73.
[28] Bardenhagen SG, Brackbill JU, Sulsky D. The material-point method for granular materials. Comput Methods App Mech Eng 2000;187(3–4):529–41.
[29] Bardenhagen SG, Guilkey JE, Roessig KM, Brackbill JU, Witzel WM, Foster JC. An improved contact algorithm for the material point method and application to stress propagation in granular material. Comput Model Eng Sci 2001;2(4):509–22.
[30] Zhang X, Sze KY, Ma S. An explicit material point finite element method for hyper velocity impact. Int J Numer Methods Eng 2006;66:689–706.
[31] Lian YP, Zhang X, Zhou X, Ma ZT. A FEMP method and its application in modeling dynamic response of reinforced concrete subjected to impact loading. Comput Methods App Mech Eng 2011;200(17–20):1659–70.
[32] Lian YP, Zhang X, Liu Y. An adaptive finite element material point method and its application in extreme deformation problems. Comput Methods App Mech Eng 2012;241–244(1):275–85.
[33] Wang B, Karuppiah V, Lu H, Roy S, Komanduri R. Two-dimensional mixed mode crack simulation using the material point. Mech Adv Mater Struct 2005;12:471–84.
[34] Wieckowski Z, Youn SK, Yeon JH. A particle-in-cell solution to the silo discharging problem. Int J Numer Methods Eng 1999;45:1203–25.
[35] Ma S, Zhang X, Lian YP, Zhou X. Simulation of high explosive explosion using adaptive material point method. Comput Model Eng Sci 2009;39(2):101–23.
[36] Johnson GR, Holmquist TJ. Evaluation of cylinder-impact test data for constitutive model constants. J Appl Phys 1988;64(8):3901–10.
[37] Seoa SW, Min OK, Lee JH. Application of an improved contact algorithm for penetration analysis in SPH. Int J Impact Eng 2008;35:578–88.
[38] Piekutowski AJ, Forrestal MJ, Poormon KL, Warren TL. Perforation of aluminum plates with ogive-nose steel rods at normal and oblique impacts. Int J Impact Eng 1996;18:877–87.
[39] Meyers MA. Dynamic behavior of materials. New York: John Wiley & Sons; 1994. p. 133.